Materials & Design 247 (2024) 113397

Contents lists available at ScienceDirect

Materials & Design

journal homepage: www.elsevier.com/locate/matdes

Microstructural evolution and 1500 °C oxidation resistance of $Mo(Al,Si)_2$ fabricated via an innovative two-step SHS-SPS technique

Nana Zhu [a,1], Lu Zhu [b,1], Baojing Zhang [a,*], Peizhong Feng [a,*], Shiheng Li [a], Philipp V. Kiryukhantsev-Korneev [c], Evgeny A. Levashov [c], Xuanru Ren [d], Xiaohong Wang [a,*]

[a] School of Materials Science and Physics, China University of Mining and Technology, Xuzhou 221116, China
[b] Department of Civil and Environmental Engineering, The Hong Kong Polytechnic University, Hong Kong 999077, China
[c] National University of Science and Technology "MISIS", Leninsky Prospect, 4, Moscow 119049, Russia
[d] Henan Key Laboratory of High Performance Carbon Fiber Reinforced Composites, Institute of Carbon Matrix Composites, Henan Academy of Sciences, Zhengzhou 450046, China

ARTICLE INFO

Keywords:
Two-step technique
$MoSi_2$
Al-alloyed ceramics
Microstructural evolution
High-temperature oxidation

ABSTRACT

An innovative two-step approach of self-propagating high-temperature synthesis (SHS) and spark plasma sintering (SPS) was developed to rapidly fabricate $MoSi_2$ and $Mo(Al,Si)_2$ ceramics for high-temperature anti-oxidation applications. The SHS process predominantly promoted the synthesis of high-purity and high-yield $MoSi_2$ and $Mo(Si,Al)_2$ phases in the alloyed powders. Subsequently, dense and crack-free $MoSi_2$ and $Mo(Al,Si)_2$ ceramics were produced using SPS. 1500 °C oxidation tests of the ceramics (100 h) revealed the formation of a protective SiO_2 oxide layer on the surface of $MoSi_2$ ceramics, while an Al-Si-O composite glassy oxide layer formed on $Mo(Si,Al)_2$ ceramics, which exhibited better thermal stability and lower oxygen permeability compared to the single SiO_2 oxide layer. However, an excessive Al content (>0.05 at.%) compromised the oxidation resistance due to the emergence of a Si-depleted $Mo_5(Si,Al)_3$ layer with inferior oxidation resistance, which was caused by the high-temperature diffusion of Si. Therefore, via this novel two-step SHS-SPS technique compact and crack-free $Mo(Si,Al)_2$ ceramics can be rapidly synthesized at high temperatures. When trace amount of Al was added (0.05 at.%), $Mo(Si_{0.95}Al_{0.05})_2$ showed optimum high-temperature oxidation resistance.

1. Introduction

Increasing demand for the properties of structural materials has been witnessed as the aerospace industry rapidly develops, and excellent high-temperature structural materials must possess good oxidation resistance, good chemical stability, and high strength to withstand extreme environments [1,2]. $MoSi_2$ is an attractive material for high-temperature structural applications, with a moderate density (6.24 g/cm^3), low thermal expansion coefficient ($8.1 \times 10^{-6}/K^{-1}$), and excellent electrical conductivity. Nowadays, potential applications of $MoSi_2$ include furnace elements and components for high-temperature heating elements, and components for jet engines and gas turbines [3], since a dense and continuous SiO_2 glass oxide layer will be formed on the surface in high-temperature oxygen-containing environments. SiO_2 possesses extremely low oxygen permeability of $\sim 10^{-9}$ cm^2/s, and it can prevent the diffusion of oxygen as a strong oxygen barrier in high-temperature environments. However, the SiO_2 oxide layer is relatively fragile and susceptible to stresses induced by mechanical stress and thermal expansion, which can lead to localized damage in the oxide layer, making more $MoSi_2$ phases exposed to air and causing an accelerated oxidation process to shorten the lifespan of the materials [4,5]. Therefore, it is urgent to strengthen the SiO_2 oxide layer to prevent its fracture, which aims to extend the lifespan of $MoSi_2$ at elevated temperatures and enhance its reliability in high-temperature applications.

Lots of investigations showed that improved high-temperature oxidation resistance can be achieved by adding suitable alloying elements to $MoSi_2$ [6–9], typically Al, Nb, Ce, Cr, etc [7,10–13]. Li et al explored the high-temperature oxidation resistance of Cr-modified $MoSi_2$ composite materials, and the results showed that the addition of Cr promoted the formation of SiO_2 protective layers at 500–900 °C, thus enhancing the oxidation resistance of $MoSi_2$ composite materials [14]. Chen et al. studied the effect of trace boron doping on the high-

* Corresponding authors.
E-mail addresses: zhangbj@cumt.edu.cn (B. Zhang), pzfeng@cumt.edu.cn (P. Feng), wxhcumt@cumt.edu.cn (X. Wang).
[1] Co-first authors. Nana Zhu and Lu Zhu contributed equally to this work.

https://doi.org/10.1016/j.matdes.2024.113397
Received 8 July 2024; Received in revised form 10 October 2024; Accepted 20 October 2024
Available online 24 October 2024

temperature oxidation behavior of $MoSi_2$ ceramic. Their findings revealed that the oxygen adsorption capacity on the $MoSi_2$ ceramic surface accelerated the rapid formation of the initial SiO_2 oxide layers at high temperatures. Boron increased the diffusion barrier energy for oxygen in the $MoSi_2$ matrix, hindering the inward diffusion of oxygen and reducing the oxidation rate [15]. Zhu et al. added some Cr and Nb elements into $MoSi_2$ and they found after oxidation at 1200 °C, the sample with added Cr and Nb exhibited a stronger affinity for oxygen than Mo, thus preferentially forming a mixed composite oxide layer, which enhanced the oxidation resistance [16]. Among these ceramics, Mo-Si-Al intermetallic compounds have been proven to be the most promising high-temperature oxidation application [17]. By partially replacing Si with Al, a protective aluminum oxide layer can be formed through an in-situ displacement reaction, thereby improving the oxidation resistance of $MoSi_2$ [18]. The formation of the Al_2O_3 oxide layer from $Mo(Si,Al)_2$ is stable and adherent, and there is a matching thermal expansion coefficient between the substrate material and the Al_2O_3 layer [5], namely: 7.4–8.6 × 10^{-6} °C^{-1} and 8.1–8.9 × 10^{-6} °C^{-1}. The Al-Si-O composite oxide layer is expected to show better stability and oxygen barrier properties than that of the single silica oxide layer. Although some studies have focused on the preparation and performance optimization of $Mo(Si,Al)_2$ materials, research on their high-temperature oxidation resistance remains relatively limited compared to other traditional high-temperature oxidation-resistant materials [19]. Therefore, further investigation into the high-temperature oxidation resistance and microstructural evolution of $Mo(Si,Al)_2$ materials is of great significance for developing high-performance, high-reliability high-temperature structural materials.

The main preparation methods of $MoSi_2$-based composite powders currently include mechanical alloying, molten salt method, sol–gel method, carbothermal reduction method, etc. [20–23]. These methods not only consume a large amount of energy but also require a long homogenization time. Additionally, some powder may undergo oxidation during the preparation process [24]. The self-propagating high-temperature synthesis (SHS) technique is a reliable method for preparing composite materials as it sustains continuous combustion by releasing heat. Compared with traditional processes, SHS involves fewer steps, shortens processing time, and has advantages of low cost and time efficiency [25]. However, ceramics prepared by SHS usually have high porosity, which seriously reduces their oxidation resistance at high temperatures because the pores provide a pathway for oxygen diffusion. Therefore, although SHS shows promise for synthesizing alloy materials with high purity and high sintering activity, a new method must be developed to prepare target ceramics using SHS powders as raw materials.

Currently, common methods for preparing bulk ceramics with high oxygen resistance include halide activated pack cementation (HAPC), hot dip silicon-plating (HDS), liquid phase sintering, slurry method, chemical vapor deposition, embedding method, and spark plasma sintering (SPS) [26–32]. Fu et al. studied the low-temperature oxidation behavior and mechanism of hot-dip aluminum and aluminum–silicon coatings on molybdenum substrate at 600 °C in static air, the growth mechanism of aluminum–silicon coatings deposited on molybdenum substrate by hot-dip plating technology, the formation of $MoSi_2$ and Si/$MoSi_2$ coatings on TZM (Mo-0.5Ti-0.1Zr-0.02C) alloy by hot dip silicon-plating method, and the improvement of oxidation resistance of TZM alloy by depositing Si-$MoSi_2$ composite coating with high silicon concentration [33]. Wang et al. used chemical vapor deposition to prepare SiC/ZrB_2-SiC/ZrB_2/SiC coatings, which showed excellent ablation resistance with a mass and linear ablation rate of only 0.27 mg/s and 0.57 mm/s after 298 s of ablation by an oxyacetylene flame [34].

In recent years, the innovative technology of spark plasma sintering (SPS) has been developed, which offers advantages such as rapid heating, short processing time, and controllable coating composition and thickness, enabling the rapid densification of ceramics [35]. Benefiting from the rapid densification characteristics during high-temperature sintering in SPS, products with extremely low porosity can be obtained. Therefore, SHS can first be applied to synthesize aluminum-alloyed $MoSi_2$ powders, and then SPS technology can be used to prepare ceramics from these powders. Regrettably, although this two-step SHS-SPS method is expected to obtain high purity, high-sintering-activity, and high-density alloyed ceramics in a short time for anti-oxidation purposes, few related investigations have been reported.

Herein, Mo, Si, and Al powders were utilized as raw materials to synthesize $MoSi_2$ and $Mo(Si,Al)_2$ powders via SHS. Subsequently, the SHSed powders were used to prepare $Mo(Si_{1-x}Al_x)_2$ (x = 0, 0.05, 0.1, 0.15, 0.2) ceramics using rapid SPS. The influence of Al content on the synthesis process and phase composition of $MoSi_2$ and $Mo(Si,Al)_2$ ceramics was studied. The morphologies and microstructural evolution of $MoSi_2$ and $Mo(Si,Al)_2$ ceramics after SPS were investigated. Furthermore, the high-temperature oxidation behavior and related anti-oxidation mechanism of Al-alloyed $MoSi_2$ at 1500 °C were also explored, which aims to develop a novel kind of $MoSi_2$-based materials for high-temperature application.

2. Experimental

2.1. Raw materials for SHS process

Molybdenum (45 μm diameter, 99.9 % purity, Beijing Licheng Innovation Metal Materials Technology Co., Ltd), silicon (75 μm diameter, 99 % purity, Tianjin Kemiou Chemical Reagent Co., Ltd.), and aluminum (25 μm diameter, 99.9 % purity, Shanghai Aladdin Bio-Chem Technology Co., Ltd.) powders were used as raw materials for SHS. They were mixed according to different atomic ratios as follows: $MoSi_2$, $Mo(Si_{0.95}Al_{0.05})_2$, $Mo(Si_{0.9}Al_{0.1})_2$, $Mo(Si_{0.85}Al_{0.15})_2$, and $Mo(Si_{0.8}Al_{0.2})_2$ using a ball-milling device (6 h, 450 rpm). Then, the mixtures were dried and cold-pressed under an applied pressure of 200 MPa for 1.5 min to form compacts (diameter of 16 mm, height of 15 mm). The SHS process was carried out in a pure argon atmosphere (99.99 %, 0.1 MPa). After SHS, the samples were taken out and crushed into powders with subsequent ball-milling process at 450 rpm for 6 h.

2.2. SPS for the fabrication of the samples

The SHSed $MoSi_2$, $Mo(Si_{0.95}Al_{0.05})_2$, $Mo(Si_{0.9}Al_{0.1})_2$, $Mo(Si_{0.85}Al_{0.15})_2$, and $Mo(Si_{0.8}Al_{0.2})_2$ powders were loaded into a graphite mold (15.5 mm diameter), and graphite foil was added between the powders and the mold to avoid high-temperature adhesion. Fabrication of ceramics was carried out via spark plasma sintering (lab-125, sinter land Inc, Japan) in a vacuum atmosphere, and the relevant parameters for SPS were given as follows: the pressure was 30 MPa, sintering temperature was 1500 °C, and the holding time was 5 min. After SPS, the samples' surfaces were polished via SiC paper to remove the residual graphite foil, and then they were washed by ultrasonic cleaning.

2.3. High-temperature oxidation at 1500 °C

The high-temperature oxidation test of the SPSed samples was carried out at 1500 °C for 0–100 h in a high-temperature furnace. Before the test, the samples were placed in alumina crucibles in the furnace for the oxidation test, and they were taken out from the furnace after oxidation. The mass changes of the samples were recorded using an electronic balance. The calculation method of the mass change is given as follows.

$$\Delta m = \frac{1}{n}\sum_{j=0}^{n}\frac{m_{t,j} - m_{o,j}}{s} \quad (1)$$

where $m_{t,j}$ is the average mass of the sample j after oxidation time t, $m_{o,j}$ is the initial mass of the sample before oxidation, n is the number of parallel samples during the experiment (n = 3), and S represents the total surface area of each original sample. Based on the recorded

changes in coating mass, the corresponding high-temperature oxidation kinetic curves were calculated, and the related oxidation mechanisms were analyzed. The diagram preparation process is illustrated in Fig. 1.

2.4. Material characterization

X-ray diffraction (XRD, Bruker D8) was used to determine the phase composition and crystalline structure of the SHSed and SPSed $MoSi_2$, Mo$(Si_{0.95}Al_{0.05})_2$, Mo$(Si_{0.9}Al_{0.1})_2$, Mo$(Si_{0.85}Al_{0.15})_2$, and Mo$(Si_{0.8}Al_{0.2})_2$. Scanning electron microscopy (SEM, Quanta 250) was utilized to observe the surface and cross-sectional morphologies of $MoSi_2$ and Al-alloyed $MoSi_2$ ceramics samples after sintering and oxidation, coupled with energy-dispersive X-ray spectroscopy (EDS, FEI Quanta 250, USA) for precise analysis of elemental content and material composition of the samples. Electron probe microanalysis (EPMA, 8050G) was employed to further analyze the elemental composition of the surface and cross-section of $MoSi_2$ and Mo$(Si,Al)_2$ ceramics after SPS sintering and high-temperature oxidation. Transmission electron microscopy (TEM, Tecnai G2 F20) was used to detect the morphology of SHSed Mo$(Si_{0.95}Al_{0.05})_2$ powder and the oxide layer after oxidation at 1500 °C for 100 h.

3. Results and discussion

3.1. Microstructure, phase composition and micromorphology

3.1.1. Phase composition and microstructure of SHSed powders

Fig. 2(a) shows the XRD patterns of SHSed Mo$(Si_{1-x}Al_x)_2$ ($x = 0$, 0.05, 0.1, 0.15, 0.2). After SHS, $MoSi_2$ and Mo$(Si,Al)_2$ phases were formed in $MoSi_2$ and Mo$(Si_{1-x}Al_x)_2$. No detectable residual raw material powders can be found after synthesis, showing SHS can fully convert the raw material powders into the target products. The addition of Al increases the combustion front temperature, which is beneficial for the self-propagating reaction between Mo and Si. The exothermic combustion reaction between Mo, Si, and Al can sustain the reaction spontaneously, and the addition of Al also suppresses the oxidation of Mo during the self-propagating reaction process. With increasing Al content, the remaining $MoSi_2$ phases disappear, indicating that Al facilitates a more complete progression of the self-propagating reaction. In the Al-alloyed $MoSi_2$ ceramics, the main phase is the Mo$(Si,Al)_2$, and the relative intensity of the Mo$(Si,Al)_2$ phase increases with increasing Al content, which is probably because Al dissolves into $MoSi_2$ after the addition, thereby making Mo$(Si,Al)_2$ phase generate with a C40 structure. As reported [36], the Mo$(Si,Al)_2$ phase has better high-temperature oxidation resistance than $MoSi_2$ (C11b), indicating the Al-alloyed is expected to have better high-temperature oxidation resistance than single $MoSi_2$.

Fig. 2(b-g) shows the TEM images of SHSed Mo$(Si,Al)_2$ powder with corresponding EDS analysis. High concentrations of Mo, Al, Si, and O elements are revealed in the SHSed Mo$(Si,Al)_2$ powders (Fig. 2 (b-e)), and these elements are observed to be uniformly distributed in the nanoparticles without any visible element segregation. The High-Resolution TEM (HRTEM) image of the powder that is represented in Fig. 2(f) shows the lattice fringes of the (200) crystal plane with a measured interplanar spacing value of $d_{(200)} = 2.01$ Å. Fig. 2(g) displays the Inverse Fast Fourier transform (IFFT) image of the region in Fig. 2(f), high concentrations of dislocations, which are common lattice defects that contribute to densification enhancement during the sintering process of ceramics [37,38], can be detected in the alloyed powders.

3.1.2. Surface morphologies of SPSed samples

The surface morphologies of $MoSi_2$ and Mo$(Si_{1-x}Al_x)_2$ ($x = 0.05$–0.2) ceramics after spark plasma sintering (SPS) are shown in Fig. 3. The surface of the SPSed samples was polished and subjected to ultrasonic cleaning. Fig. 3(a) reveals that $MoSi_2$ ceramics are not dense after high-temperature sintering as some microcracks and pores can be detected on the surface. Gray, white, and black phases are the main phases in $MoSi_2$ sample, and they are indicated to be $MoSi_2$, Mo_5Si_3, and SiO_2, respectively, according to the EDS analysis, respectively. As shown in Fig. 3(b-e), Mo$(Si_{1-x}Al_x)_2$ ($x = 0.05$–0.2) ceramics exhibit a dense and intact microstructure after sintering. The main phases of Al-doped $MoSi_2$ samples are Mo$(Si,Al)_2$, Mo_5Si_3, and Al_2O_3. According to references [39–43], SiO_2 and Al_2O_3 were also detected after the SPS process, and this is attributed to the slight oxidation of $MoSi_2$ and Al during SPS. Among the samples, Mo$(Si_{0.95}Al_{0.05})_2$ exhibits the most uniform microstructure. To further examine the phase distribution of the ceramics after SPS treatment, Fig. 4 provides surface electron probe microanalysis (EPMA) of the $MoSi_2$, Mo$(Si_{0.95}Al_{0.05})_2$, and Mo$(Si_{0.8}Al_{0.2})_2$ ceramics after SPS. No significant pores or cracks are observed in any of the SPS-treated ceramics, and all phases in the Mo$(Si,Al)_2$ ceramics are uniformly distributed, indicating that SPS facilitates the production of dense and intact Mo$(Si,Al)_2$ ceramics.

3.2. High-temperature oxidation resistance of $MoSi_2$ and Al-alloyed $MoSi_2$

3.2.1. Phase composition

Fig. 5 shows the XRD patterns of Mo$(Si_{1-x}Al_x)_2$ ($x = 0$–0.2) after oxidation at 1500 °C for 1, 20, and 100 h. From Fig. 5(a), it can be seen that after oxidation at 1500 °C for 1 h, a small amount of SiO_2 phase appears on the surface of $MoSi_2$, along with a significant presence of $MoSi_2$ phase. After oxidation for 1 h, in all Al-alloyed ceramics, besides Mo$(Si,Al)_2$ phase, SiO_2, Al_2O_3, and a small amount of Mo_5Si_3 phases are also detected, which is caused by the oxidation of Mo$(Si,Al)_2$. From Fig. 5(b), it can be seen that as the oxidation time extends to 20 h, although the surface phase composition of $MoSi_2$ and the Al-alloyed ceramics remains unchanged, some peaks like $MoSi_2$ and Mo$(Si,Al)_2$ disappear due to continuous oxidation. The relative intensities of SiO_2 and Al_2O_3 also increase with the oxidation time [36]. After oxidation for

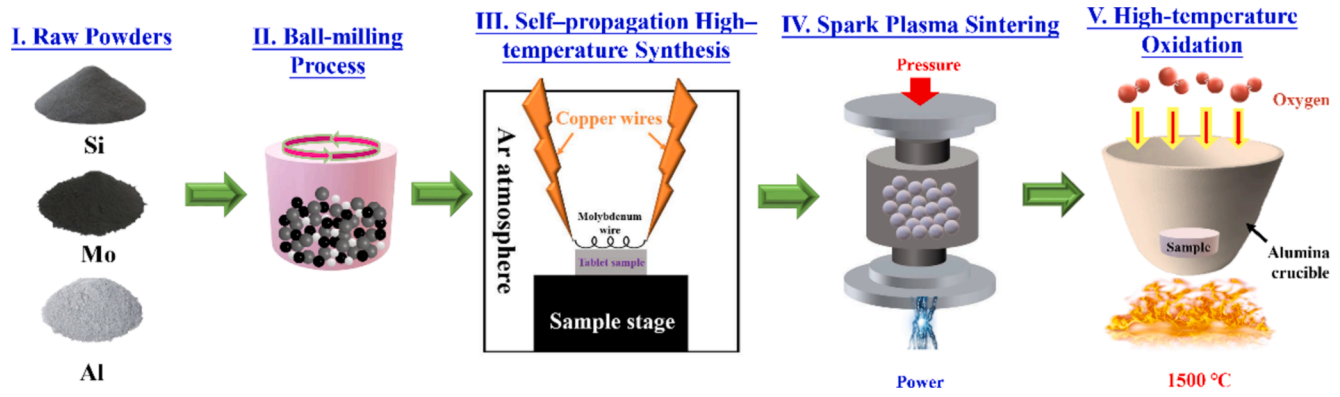

Fig. 1. Illustration diagram of the preparation and 1500 °C oxidation of Al-alloyed $MoSi_2$.

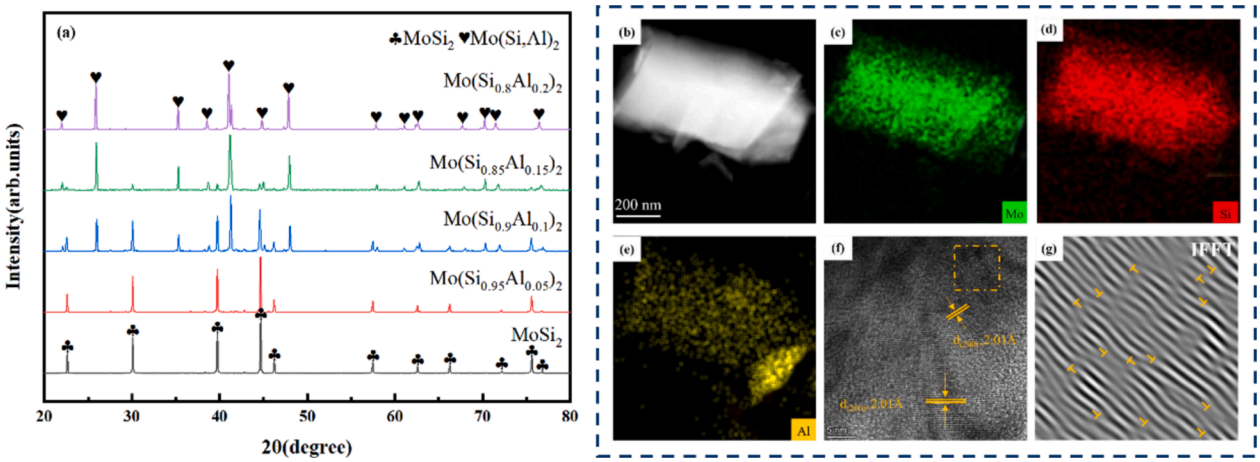

Fig. 2. (a) XRD patterns of $Mo(Si_{1-x}Al_x)_2$ ($x = 0$–0.2) after SHS; (b-e) TEM, (f) HRTEM, and (g) IFFT images with EDS analysis of $Mo(Si_{0.95}Al_{0.05})_2$ powder synthesized via SHS (b-h).

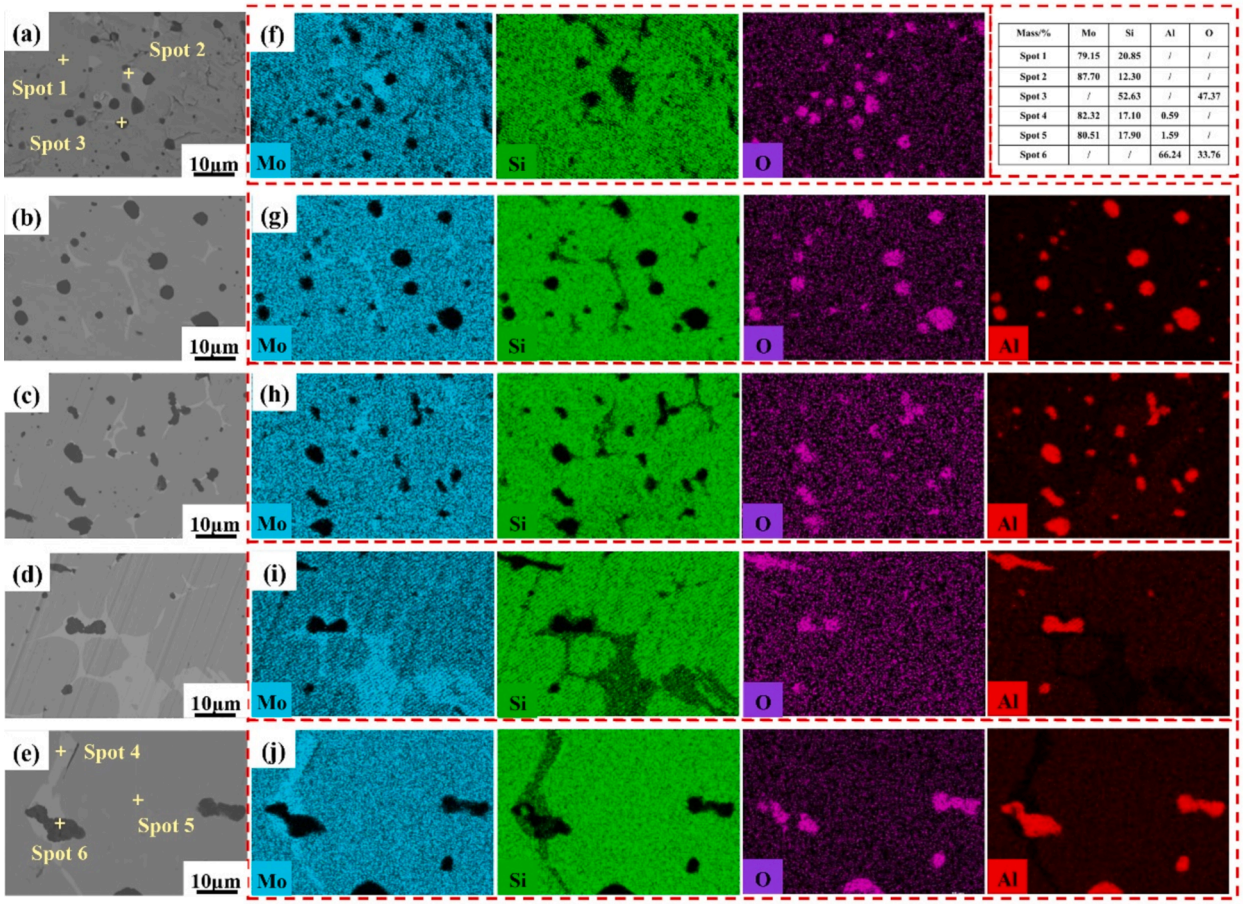

Fig. 3. Surface morphologies and EDS analysis of ceramics after SPS sintering: (a) $MoSi_2$, (b) $Mo(Si_{0.95}Al_{0.05})_2$, (c) $Mo(Si_{0.9}Al_{0.1})_2$, (d) $Mo(Si_{0.85}Al_{0.15})_2$, (e) $Mo(Si_{0.8}Al_{0.2})_2$, (f-j) EDS results.

100 h, the XRD patterns of $MoSi_2$ and $Mo(Si,Al)_2$ ceramics are shown in Fig. 5(c). The surface phase composition of $MoSi_2$ and the Al-alloyed ceramics remains unchanged, The surface of $MoSi_2$ is mainly composed of $MoSi_2$ and SiO_2, while the surface of the alloyed ceramics is mainly composed of Al_2O_3, $Mo(Si,Al)_2$, and SiO_2 [37,38]. From Fig. 2, it can be seen that after SHS, a small amount of $MoSi_2$ appears in the Al-alloyed ceramic samples, while the main phase after oxidation is $Mo(Si,Al)_2$. This is because SHS is a rapid preparation process that occurs quickly within an extremely short duration. The SHS process is prone to cause the formation of supersaturated solid solution, thus resulting in the generation of non-equilibrium phases [44–46]. However, during the SPS process with relatively long sintering time, the non-equilibrium phase will be transformed into an equilibrium state, and $Mo(Si_{0.9}Al_{0.1})_2$ that possesses C11b and C40 crystal structures will be generated, thereby promoting the formation of $Mo(Si,Al)_2$ phase (Fig. 5) [47–49].

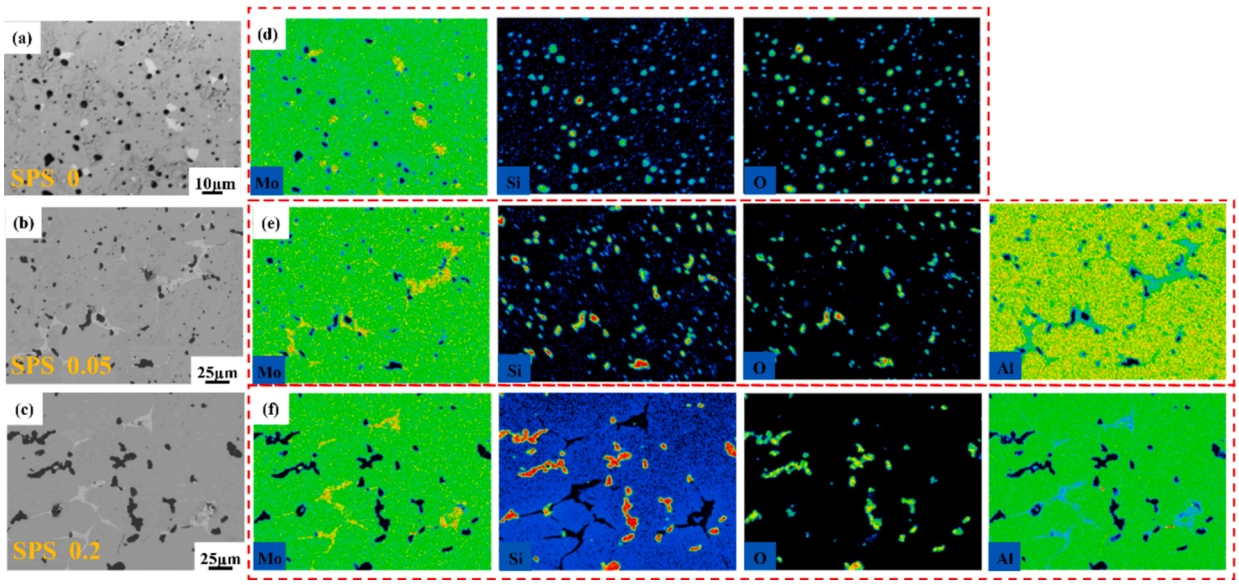

Fig. 4. Surface EPMA analysis of ceramics after SPS sintering: (a) $MoSi_2$, (b) $Mo(Si_{0.95}Al_{0.05})_2$, (c) $Mo(Si_{0.8}Al_{0.2})_2$, (d-f) EPMA results.

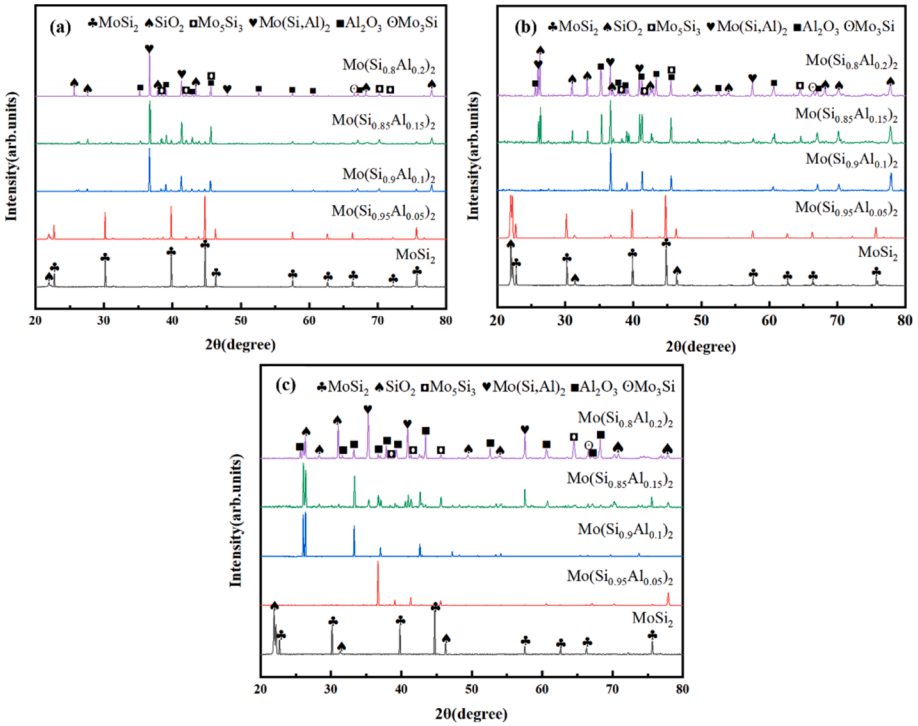

Fig. 5. XRD patterns of $Mo(Si_{1-x}Al_x)_2$ (x = 0–0.2) ceramics after oxidation at 1500°C: (a) 1 h, (b) 20 h and (c) 100 h.

According to the XRD results, the mian phases in $MoSi_2$ after oxidation at 1500 °C are SiO_2, Mo_5Si_3, and Mo_3Si. The oxidation products of $Mo(Si_{1-x}Al_x)_2$ (x = 0.05–0.2) ceramics are mainly composed of SiO_2, Al_2O_3, and Mo_5Si_3. The oxidation process of $Mo(Si_{1-x}Al_x)_2$ (x = 0–0.2) ceramics at 1500 °C can be summarized by the following reactions [33,50,51].

$$5/7MoSi_2 + O_2(g) = 1/7Mo_5Si_3 + SiO_2 \quad (2)$$

$$2/7MoSi_2 + O_2(g) = 2/7MoO_3 + 4/7SiO_2 \quad (3)$$

$$4/3Mo_5Si_3 + O_2(g) = 5/4Mo_3Si + SiO_2 \quad (4)$$

$$2/21Mo_5Si_3 + O_2(g) = 10/21MoO_3 + 6/21SiO_2 \quad (5)$$

$$2/11Mo_3Si + O_2(g) = 6/11MoO_3 + 2/11SiO_2 \quad (6)$$

$$4/3Al + O_2(g) = 2/3Al_2O_3 \quad (7)$$

$$Si + O_2(g) = SiO_2 \quad (8)$$

Fig. 6 shows the ΔG^θ change curves of the oxidation reaction with oxidation temperature. The ΔG^θ values of all oxidation reactions are shown to be negative, indicating that these reactions are spontaneous during the oxidation process [33]. Among all the equations, the ΔG^θ value of Equation (7) is the most negative, which indicates that

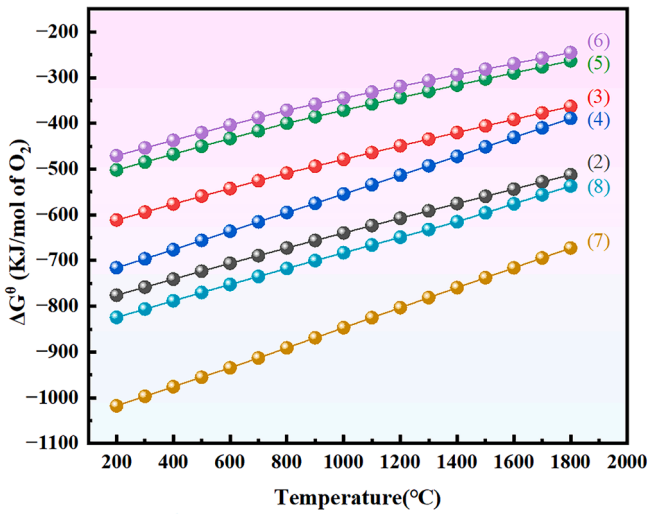

Fig. 6. The change curves of Gibbs free energy (ΔG^{θ}) of oxidation reactions with temperature for $Mo(Si_{1-x}Al_x)_2$ (x = 0–0.2) ceramics.

aluminum has the highest affinity with oxygen and is most likely to be oxidized preferentially [4]. According to the oxygen potential diagram, it can be further verified that Al_2O_3 will form preferentially over SiO_2, where the partial substitution of silicon with aluminum led to the formation of a protective alumina layer through an in-situ replacement reaction, thereby improving the oxidation resistance of the ceramics. Therefore, aluminum located at the grain boundary on the surface is preferentially oxidized to Al_2O_3 at the initial stage of oxidation. The oxidation of $MoSi_2$ can be described by Equations (2) and (3). Thermodynamic calculations show that the ΔG^{θ} of Equation (2) is lower than that of Equation (3), indicating that $MoSi_2$ will be preferentially oxidized to Mo_5Si_3. Thus, Mo_5Si_3 phases are observed on the coating surface during the middle oxidation stage. As oxidation time increases, a continuous oxide layer gradually forms on the surface, significantly reducing the diffusion rate of oxygen into the ceramics. This leads to the further oxidation of Mo_5Si_3 into Mo_3Si in the silicon layer with low oxygen content and complete oxidation to MoO_3 on the surface of the oxide layer with high oxygen content, as shown in Equations (4) and (5), respectively. When the oxygen partial pressure is high enough, Mo_3Si will eventually be oxidized to MoO_3, as shown in Equation (6). The generated MoO_3 (at 800 °C) has a relatively low melting point and volatilizes intensely in the high-temperature environment of 1500 °C, resulting in the absence of MoO_3 diffraction peaks as shown in Fig. 5.

3.2.2. *Surface and cross-sectional morphology analysis*

Fig. 7 shows the surface SEM images of $Mo(Si_{1-x}Al_x)_2$ (x = 0–0.2) ceramics after oxidation at 1500 °C for 1 h. A glassy oxide layer forms on the $MoSi_2$ surface and it is mainly composed of SiO_2 by EDS. The formation of this moss-like oxide layer is because SiO_2, which is produced by $MoSi_2$, typically exhibits a low viscosity and a high equilibrium vapor pressure, making it prone to evaporating at high temperatures [52]. Similarly, after oxidation of 1 h, a glassy oxide layer also generates on $Mo(Si_{0.95}Al_{0.05})_2$ surface with the observation of the white "grain boundary ridges" in the oxide layer which are considered to be preliminary evidence of Al diffusion along grain boundaries to form the oxides [4]. The SiO_2 oxide layer is relatively fragile and susceptible to stress caused by mechanical stress and thermal expansion, the Al-Si-O composite layer formed on $Mo(Si_{0.95}Al_{0.05})_2$ can effectively inhibit the formation of brittle SiO_2, playing a dual-layer reinforcement role at elevated temperatures. In $Mo(Si_{1-x}Al_x)_2$ system, Al is preferentially oxidized in the early stages of oxidation. This reduces the reactivity of Al in the substrate, allowing for the oxidation of silicon and resulting in the formation of a composite oxide layer. However, no complete oxide layer is generated on the surface of the ceramics as the Al content exceeds 0.05 %, indicating that excessive addition of Al is not beneficial for the formation of a continuous and dense oxide layer in a short period. Compared with other samples after oxidation for 1 h, the Al-Si-O composite oxide layer formed on $Mo(Si_{0.95}Al_{0.05})_2$ exhibits better thermal stability and oxidation resistance.

Fig. 8 represents the cross-sectional SEM images of $Mo(Si_{1-x}Al_x)_2$ (x = 0–0.2) after oxidation of 1 h. As 1 h is too short for oxidation, relatively thin layers form on the surface of $MoSi_2$ and $Mo(Si_{0.95}Al_{0.05})_2$ after oxidation. When the Al content increases, rough and uneven oxide layers are generated on the surface of $Mo(Si_{1-x}Al_x)_2$ (x = 0.1, 0.15, 0.2) ceramics due to the reaction of Al with oxygen to form Al_2O_3 and SiO_2 during the high-temperature oxidation. EDS results also prove that the oxide layer on the surface of Al-alloyed samples are made up of Al, Si, and O. With increasing Al content, the proportion of Al_2O_3 increases, resulting in a rougher morphology of the oxide layer, and this can be attributed to the larger particle size and uneven distribution of Al_2O_3. However, a thin and obvious silicon-depleted layer can be also detected to be formed between the $Mo(Si_{1-x}Al_x)_2$ (x = 0.15, 0.2) and oxide layer, indicating that excessive Al content accelerates the diffusion of Si from $Mo(Si,Al)_2$ to form a silicon-depleted layer $Mo_5(Si,Al)_3$ [4].

The surface morphologies and corresponding EDS analysis of $Mo(Si_{1-x}Al_x)_2$ (x = 0–0.2) ceramics after oxidation of 20 h at 1500 °C are shown in Fig. 9. After oxidation of 20 h, A distinct and continuous oxide layer without any cracks formed on the surface of $MoSi_2$, $Mo(Si_{0.95}Al_{0.05})_2$, and $Mo(Si_{0.9}Al_{0.1})_2$. With the increase of Al content, rough oxide layers appear on $Mo(Si_{0.85}Al_{0.15})_2$ and $Mo(Si_{0.8}Al_{0.2})_2$ ceramics after oxidation, and they are mainly made up of Al_2O_3 and SiO_2 by EDS results. The formation of the Al_2O_3 primarily involves oxygen diffusion inward along the grain boundaries and Al diffusion outward along the grain boundaries. The outward diffusion of Al promotes the formation of Al_2O_3 at the interface, leading to the replacement of SiO_2 by Al_2O_3 until Al_2O_3 completely covers the sample surface [53–55]. Fig. 10 shows the TEM and HRTEM images of the oxide layer on $Mo(Si_{0.95}Al_{0.05})_2$ after oxidation at 1500 °C for 20 h, and it represents the lattice fringes of the (113) crystal plane with a measured interplanar spacing value of $d_{(113)}$ = 3.01 Å, which also proves the existence of Al_2O_3 phase by the oxidation reaction.

The cross-sectional morphologies and EDS analysis of $Mo(Si_{1-x}Al_x)_2$ (x = 0–0.2), after oxidation for 20 h are provided in Fig. 11. As shown in Fig. 11(a), the silica oxide layer, can still be observed on $MoSi_2$, while Al-Si-O oxide layer is observed on $Mo(Si_{0.95}Al_{0.05})_2$. The internal layers of the ceramics maintain good metallurgical bonding and thermal compatibility without any debonding or cracks. Besides the formation of oxide layers on $Mo(Si_{1-x}Al_x)_2$ (x = 0.1, 0.15, 0.2), a silicon-depleted layer was also generated between the Al-Si-O composite oxide layer and substrate. Based on the EDS analysis, the silicon-depleted layer is identified as $Mo_5(Si,Al)_3$, and the silicon-depleted layer formation is attributed to the diffusion of Si from $Mo(Si,Al)_2$ [56]. In addition, with increasing Al content, the silicon-depleted layer becomes thicker, which is mainly because Al is more reactive during high-temperature oxidation, which promotes the diffusion of silicon to form a silicon-depleted layer, indicating that more silicon is transferred to the surface of the oxide and resulting in a thicker silicon-depleted layer. Compared to the silicon-depleted layer after oxidation of 1 h (Fig. 8), the thickness of the silicon-depleted layer increases. The increased thickness of the silicon-depleted layer with increasing oxidation time is due to the accelerated diffusion rates of silicon and Al, which leads to more silicon diffusing outward from $Mo(Si,Al)_2$ to form a silicon-depleted layer on the oxide surface. Consequently, as the oxidation time increases, the thickness of the silicon-depleted layer correspondingly increases [4]. However, the oxidation resistance of $Mo_5(Si,Al)_3$ is poorer than $Mo(Si,Al)_2$ [5], and the excessive growth of the $Mo_5(Si,Al)_3$ silicon-depleted layer will decrease the oxidation inhibition ability of the ceramics. To better analyze the elemental distribution in the oxidized ceramic samples, the cross-sectional EPMA images of $Mo(Si_{1-x}Al_x)_2$ (x = 0, 0.05, 0.2), after 20

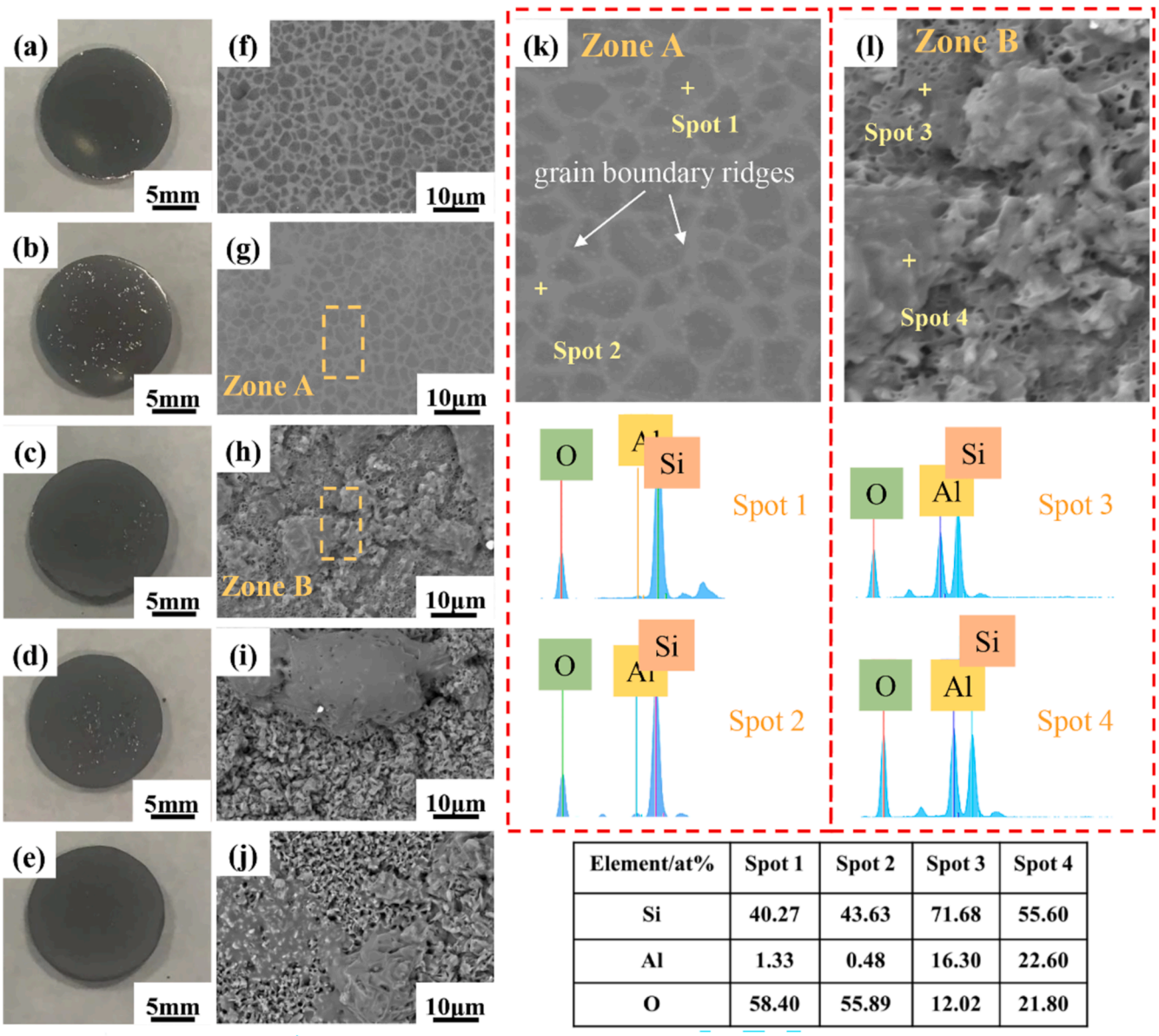

Element/at%	Spot 1	Spot 2	Spot 3	Spot 4
Si	40.27	43.63	71.68	55.60
Al	1.33	0.48	16.30	22.60
O	58.40	55.89	12.02	21.80

Fig. 7. Surface morphologies and EDS analysis of the ceramics after oxidation at 1500 ℃ for 1 h: (a) $MoSi_2$, (b) $Mo(Si_{0.95}Al_{0.05})_2$, (c) $Mo(Si_{0.9}Al_{0.1})_2$, (d) $Mo(Si_{0.85}Al_{0.15})_2$, (e) $Mo(Si_{0.8}Al_{0.2})_2$, (f- l) EDS results.

h of oxidation are provided in Fig. 12. As shown in Fig. 11(a, b, e), dense glassy oxide layers that formed by the reaction of $MoSi_2$ (or $Mo(Si,Al)_2$), can be observed on the ceramics. Through EPMA analysis, a thin layer of SiO_2 (~ 4μm) can be seen on the surface of $MoSi_2$, while a tightly bonded Al-Si-O composite layer formed on $Mo(Si_{0.95}Al_{0.05})_2$. However, the oxide layer of $Mo(Si_{0.8}Al_{0.2})_2$ is uneven and rough, and this is because the addition of Al may result in uneven grain sizes, which macroscopically manifests as a rough surface [10]. The EPMA results of oxidized Mo $(Si_{0.8}Al_{0.2})_2$ always prove the formation of $Mo_5(Si,Al)_3$ silicon-depleted layer between the Al-Si-O composite oxide layer and substrate, thus displaying its relatively poorer high-temperature oxidation resistance. Thus, compared with other samples, $Mo(Si_{0.95}Al_{0.05})_2$ possesses better anti-oxidation properties at elevated temperatures.

Fig. 13 shows the surface SEM images of $Mo(Si_{1-x}Al_x)_2$ ($x = 0$–0.2) ceramics after oxidation at 1500 °C for 100 h. As shown in Fig. 13(a,b), the surfaces of both $MoSi_2$ and $Mo(Si_{0.95}Al_{0.05})_2$ are covered by dense and smooth protective oxide layers without any cracks or debonding even after 100 h of oxidation. In Fig. 13(h-j), the oxide layers on the oxidized $Mo(Si_{1-x}Al_x)_2$ ($x = 0.1$–0.2) all display a needle-like Al_2O_3 by EDS, and it is attributed to the diffusion of oxygen along the Al formation. It is noticed that fracture occurs in both $Mo(Si_{0.85}Al_{0.15})_2$ and $Mo(Si_{0.8}Al_{0.2})_2$ ceramics after 100 h of oxidation, indicating that excessive Al content will cause the deterioration of the anti-oxidation properties. Compared with other ceramics, $Mo(Si_{0.95}Al_{0.05})_2$, in which only tiny amounts of Al are doped, shows better oxidation resistance and the explanation is given as follows. By adding tiny Al, the crystal structure of $MoSi_2$ gradually transforms into the hexagonal C40 type. Compared to the C11b structure of $MoSi_2$, the C40-$MoSi_2$ exhibits better crystal stability and structural densification. Additionally, C40-$MoSi_2$ possesses higher crystal symmetry and a denser lattice arrangement than C11b-$MoSi_2$, making the oxygen difficult to penetrate the ceramic, thus causing fewer oxidation reactions at elevated temperatures. In addition, Al atoms replace silicon atoms in the crystal lattice of $MoSi_2$, which increases the proportion of metallic bonds and improves the symmetry of the crystal structure, thus making better high-temperature oxidation obtained by $Mo(Si_{0.95}Al_{0.05})_2$. However, excessive Al causes the transformation of $Mo(Si,Al)_2$ into an orthorhombic C54 structure, thereby worsening the oxidation resistance at 1500 °C [50,57].

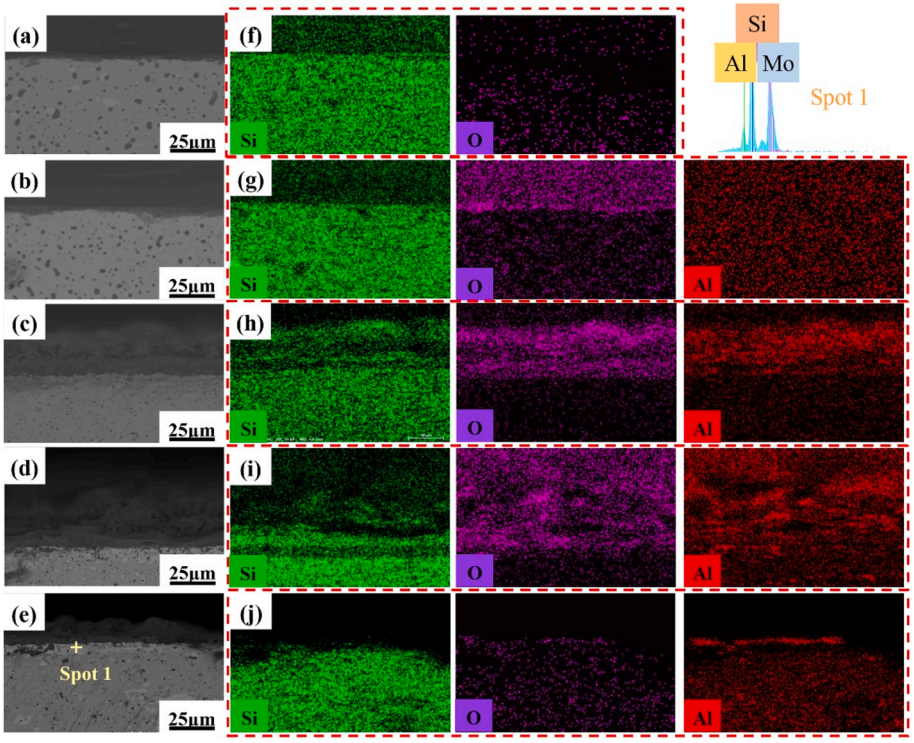

Fig. 8. Cross-sectional morphologies and EDS results of the ceramics after oxidation at 1500 ℃ for 1 h:(a) $MoSi_2$, (b) $Mo(Si_{0.95}Al_{0.05})_2$, (c) $Mo(Si_{0.9}Al_{0.1})_2$, (d) $Mo(Si_{0.85}Al_{0.15})_2$, (e) $Mo(Si_{0.8}Al_{0.2})_2$, (f-j) EDS results.

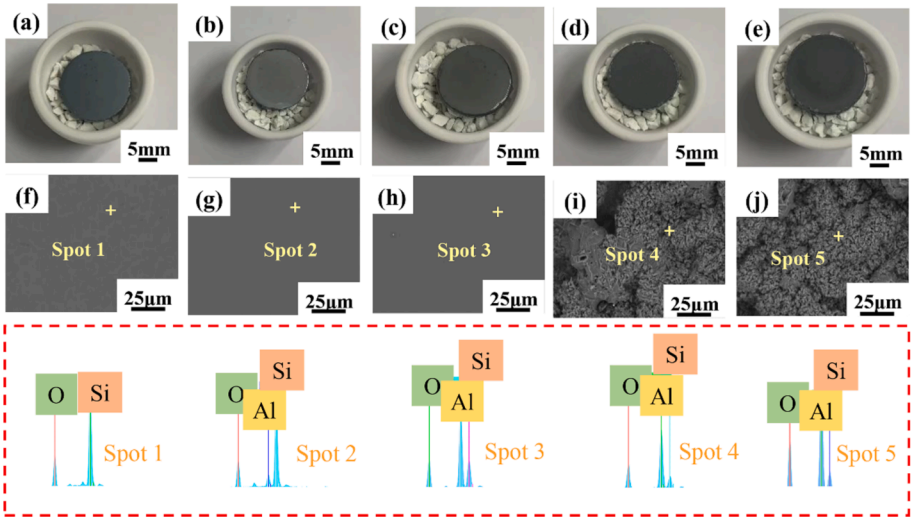

Fig. 9. Surface morphology of ceramics after oxidation at 1500 ℃ for 20 h: (a) $MoSi_2$, (b) $Mo(Si_{0.95}Al_{0.05})_2$, (c) $Mo(Si_{0.9}Al_{0.1})_2$, (d) $Mo(Si_{0.85}Al_{0.15})_2$, (e) $Mo(Si_{0.8}Al_{0.2})_2$, (f-j) EDS results.

Fig. 14 shows the cross-sectional SEM morphology of $MoSi_2$ and $Mo(Si_{0.95}Al_{0.05})_2$ after 100 h of oxidation. As shown in Fig. 14(a), the oxide layer of $MoSi_2$ thickens as the oxidation time increases. After long-term oxidation at high temperatures, the oxide layer of $MoSi_2$ is still well-bonded with the substrate with no visible peeling or gaps between the layers, indicating good interlayer compatibility after long-term oxidation at elevated temperatures. The thickness of the Al-Si-O composite oxide layer of $Mo(Si_{0.95}Al_{0.05})_2$ is also increased after 100 h of oxidation increases by the formation of Al_2O_3 and SiO_2, and excellent adhesion between the oxide layer and substrate is obtained. The cross-section EPMA analysis of $Mo(Si_{0.95}Al_{0.05})_2$ after 100 h of oxidation at 1500 °C shown in Fig. 14(c) also proves the formation of a dense and smooth oxide layer. Interestingly, an extremely thin silicon-depleted layer, which is made up of the mixtures of Mo_5Si_3 and $Mo_5(Si,Al)_3$ is formed under the oxide layer. Although the formation of Mo_5Si_3 and $Mo_5(Si,Al)_3$ is not beneficial for the improvement of oxidation resistance due to the poor oxidation resistance of Mo_5Si_3, its thickness is extremely low after long-term high-temperature oxidation at 1500 °C, and it also strengthens the bonding between the substrate and oxide layer, thus greatly reducing the risk of cracks and debonding between layers. However, as excessive Al is added, a thick $Mo_5(Si,Al)_3$ silicon-depleted layer is detected in Fig. 15. Large amounts of $Mo_5(Si,Al)_3$ with poorer oxidation resistance will be detrimental to the high-temperature oxidation resistance. Therefore, when the Al content is excessively

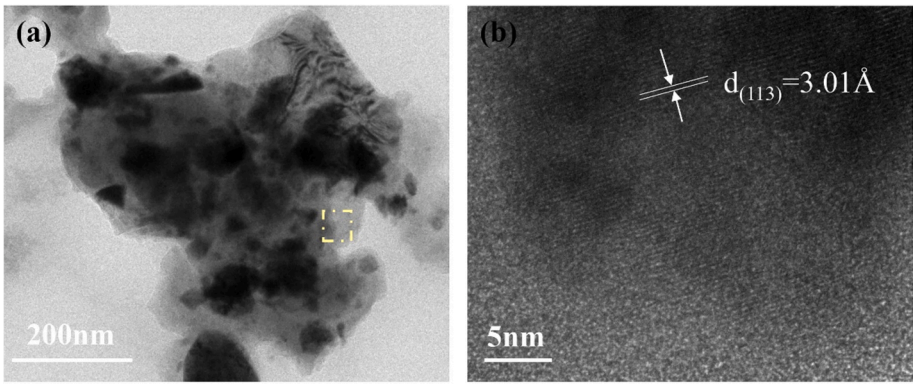

Fig. 10. (a) TEM and (b) HRTEM images of the oxide layer of $Mo(Si_{0.95}Al_{0.05})_2$ after oxidation at 1500 ℃ for 20 h.

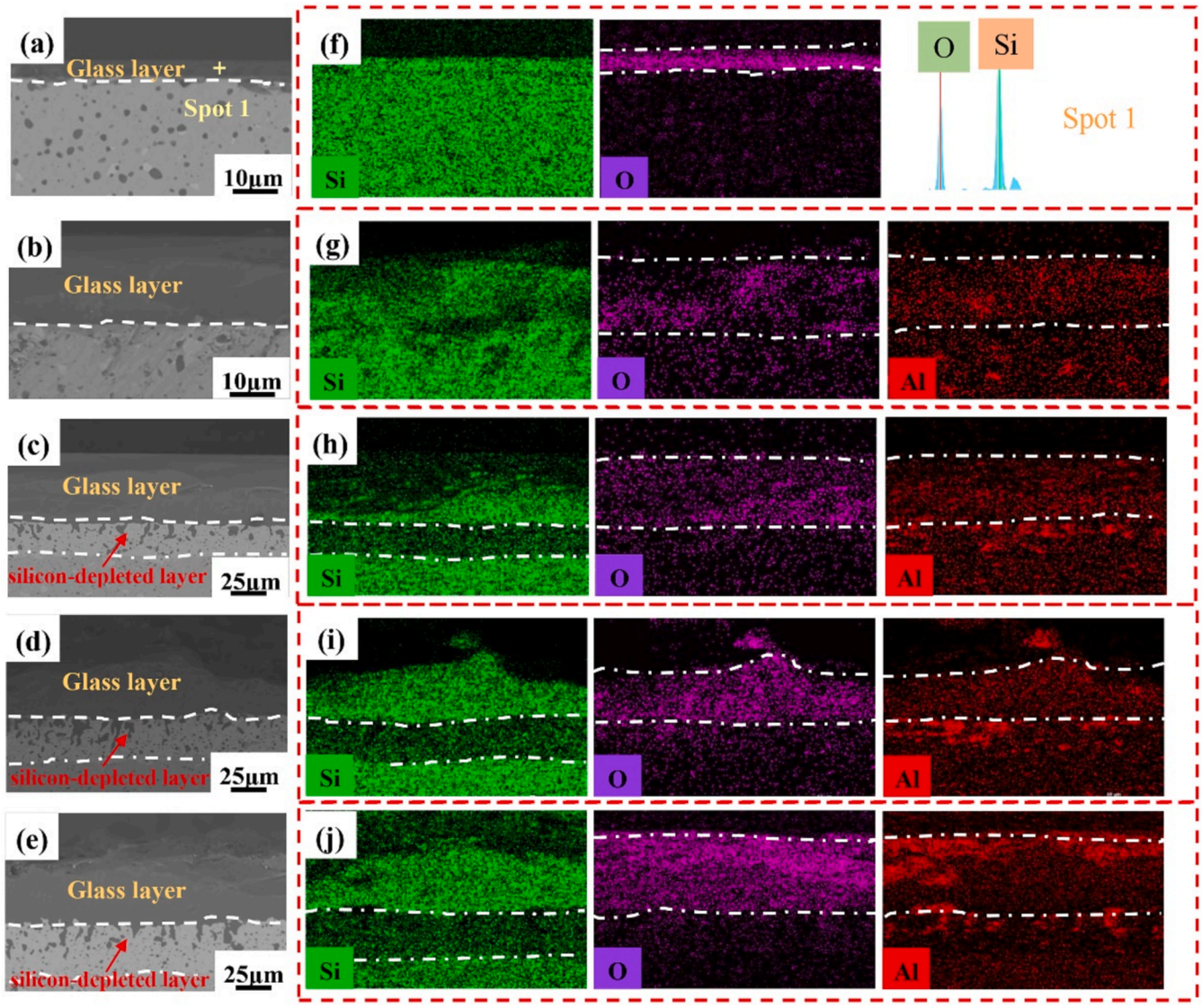

Fig. 11. Cross-sectional morphology and EDS results of the ceramics after oxidation at 1500 ℃ for 20 h: (a) $MoSi_2$, (b) $Mo(Si_{0.95}Al_{0.05})_2$, (c) $Mo(Si_{0.9}Al_{0.1})_2$, (d) $Mo(Si_{0.85}Al_{0.15})_2$, (e) $Mo(Si_{0.8}Al_{0.2})_2$, (f-j) EDS results.

added, although the continuous oxide layer is completely formed, more consumption of substrate materials will be caused by the continuous formation of the silicon-depleted layer under the same oxidation conditions, thereby deteriorating the high-temperature oxidation resistance of the ceramic system.

The mass gain of $Mo(Si_{1-x}Al_x)_2$ (x = 0–0.2) ceramics after oxidation at 1500 °C for 0–100 h is shown in Fig. 16(a). $MoSi_2$ and $Mo(Si_{0.95}Al_{0.05})_2$ ceramics exhibit rapid mass gain during the Rapid

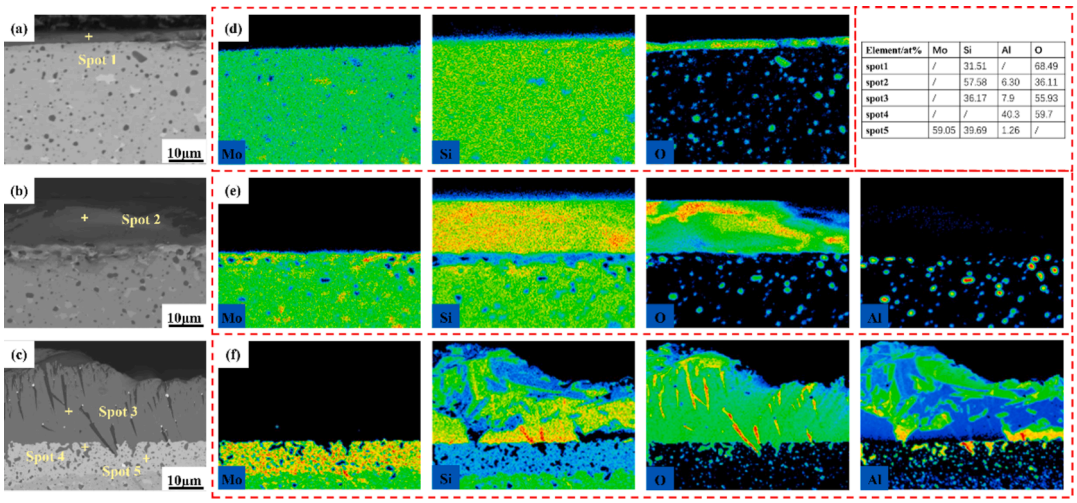

Fig. 12. Cross-sectional morphologies and EPMA analysis of the ceramics after oxidation at 1500 ℃ for 20 h: (a) $MoSi_2$, (b) $Mo(Si_{0.95}Al_{0.05})_2$, (c) $Mo(Si_{0.8}Al_{0.2})_2$, (d-f) EPMA results.

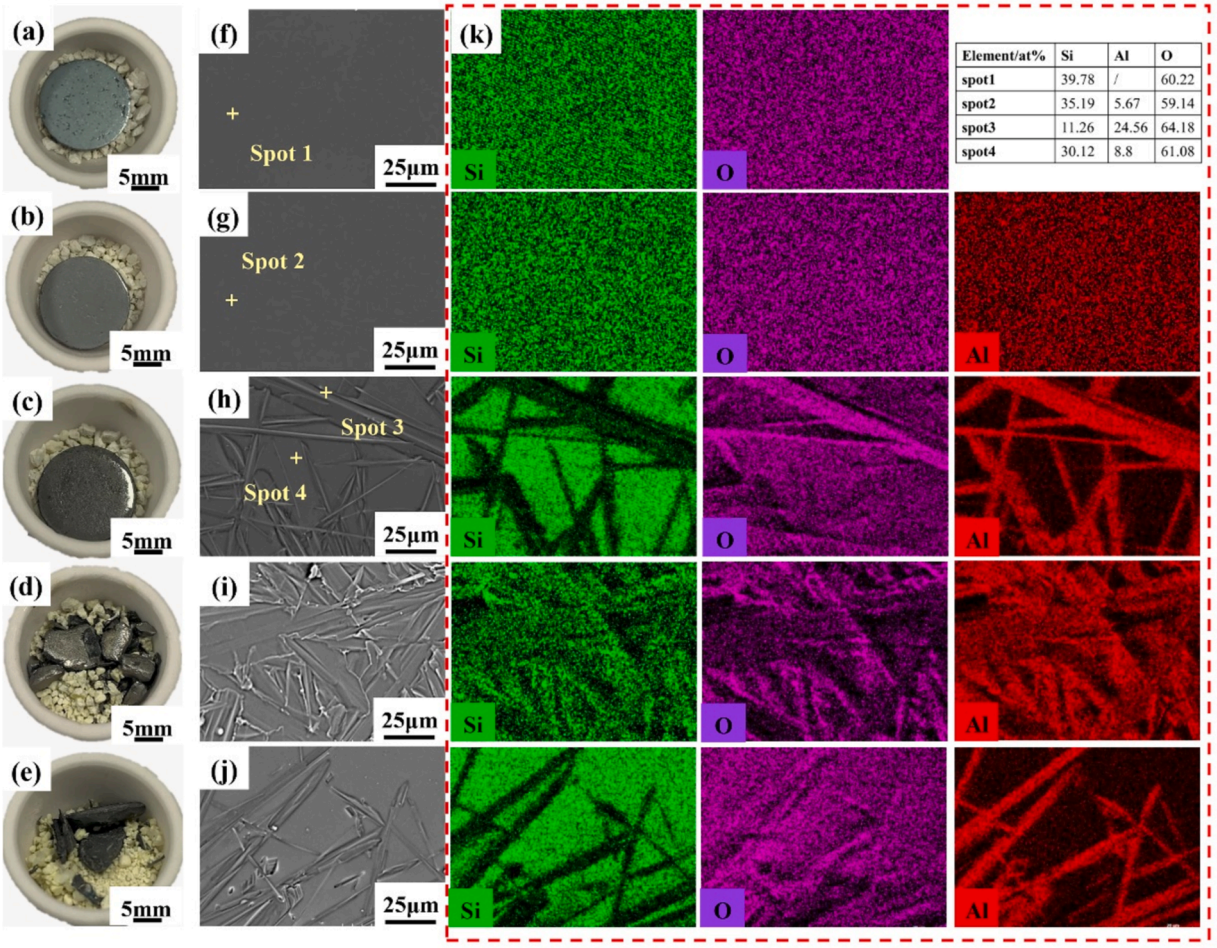

Fig. 13. Surface morphologies and EDS analysis of the ceramics after oxidation at 1500 ℃ for 100 h: (a) $MoSi_2$, (b) $Mo(Si_{0.95}Al_{0.05})_2$, (c) $Mo(Si_{0.9}Al_{0.1})_2$, (d) $Mo(Si_{0.85}Al_{0.15})_2$, (e) $Mo(Si_{0.8}Al_{0.2})_2$, (f-j) EDS results.

Oxidation Stage (0–20 h) because the exposed $MoSi_2$ surface must undergo rapid and harsh oxidation during this stage to form a SiO_2 oxide layer, while $Mo(Si_{1-x}Al_x)_2$ (x = 0.05–0.2) undergoes oxidation to generate Al-Si-O composite oxide layer. As the oxidation time increases (Slow Oxidation Stage, 20–100 h), sharp mass loss starts to occur in the high Al-containing samples ($Mo(Si_{0.85}Al_{0.15})_2$、$Mo(Si_{0.8}Al_{0.2})_2$), which is probably due to the oxidation of the silicon-depleted layers in Fig. 8, which will produce volatile MoO_3. As shown in Fig. 16(b), which represents the mass change of $Mo(Si_{1-x}Al_x)_2$ (x = 0–0.1) at 1500 °C for 0–100 h. The $Mo(Si_{0.9}Al_{0.1})_2$ ceramic exhibits mass loss, while the Mo

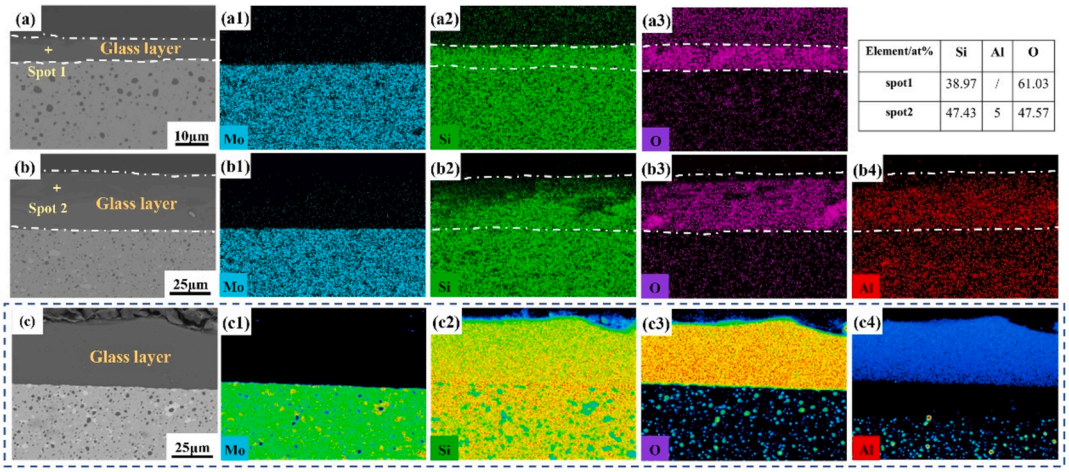

Element/at%	Si	Al	O
spot1	38.97	/	61.03
spot2	47.43	5	47.57

Fig. 14. Cross-sectional morphologies and EPMA analysis of the ceramics after oxidation at 1500 ℃ for 100 h: (a) $MoSi_2$ EDS, (b) $Mo(Si_{0.95}Al_{0.05})_2$ EDS, (c) $Mo(Si_{0.95}Al_{0.05})_2$ EPMA.

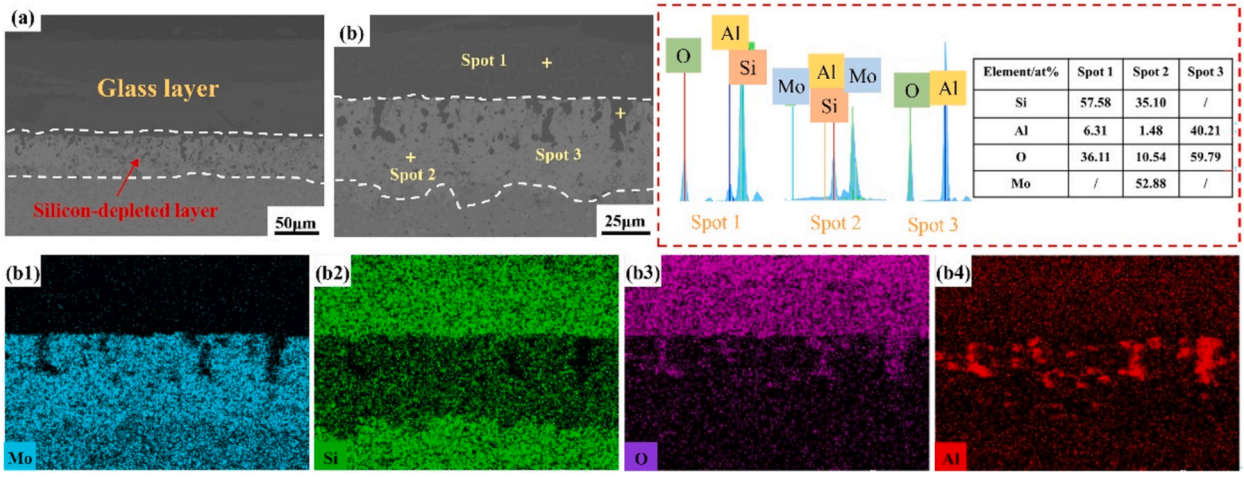

Element/at%	Spot 1	Spot 2	Spot 3
Si	57.58	35.10	/
Al	6.31	1.48	40.21
O	36.11	10.54	59.79
Mo	/	52.88	/

Fig. 15. Cross-sectional morphology and EDS analysis of $Mo(Si_{0.9}Al_{0.1})_2$ ceramics after oxidation at 1500 ℃ for 100 h: (a, b) Cross-sectional morphology, (b1-b4) EDS results.

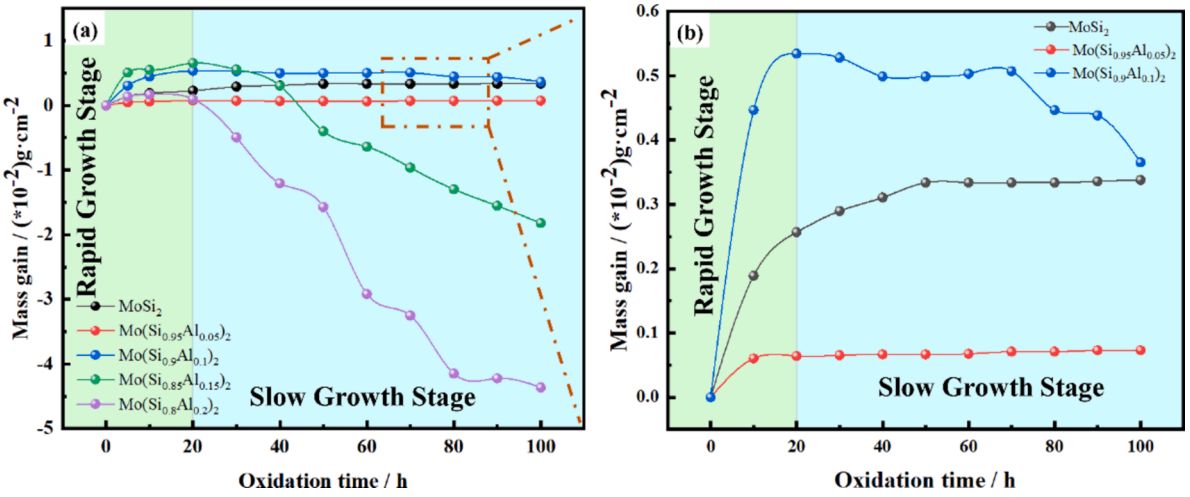

Fig. 16. Mass change curves of the ceramics after oxidation: (a) $Mo(Si_{1-x}Al_x)_2$ (x = 0–0.2), (b) $Mo(Si_{1-x}Al_x)_2$ (x = 0–0.1).

$(Si_{0.95}Al_{0.05})_2$ ceramic shows a relatively slow mass gain. The oxidation rate of $MoSi_2$ is believed to be controlled by the inward diffusion of O_2 molecules through amorphous SiO_2, while the oxidation rate of $Mo(Si_{1-x}Al_x)_2$ ($x = 0.05$–0.2) is attributed to the outward diffusion of Al^{3+} ions and the inward diffusion of O^{2-}. During the oxidation stage, the oxide layer formed on the surface of $Mo(Si_{1-x}Al_x)_2$ ($x = 0$, 0.05, 0.1) ceramics can effectively inhibit the penetration of oxygen, thereby slowing down the change in the quality of ceramics. Compared to the five ceramics before oxidation, after 100 h of high-temperature oxidation, the mass increases of $Mo(Si_{1-x}Al_x)_2$ ($x = 0$, 0.05, 0.1) ceramics are approximately 0.3382, 0.0729, 0.3654 g/cm^2, respectively. Compared with $MoSi_2$ and other Al-alloyed samples under the same oxidation conditions, the lowest mass gain is obtained by $Mo(Si_{0.95}Al_{0.05})_2$ ceramic indicating the Al-alloyed ceramics with tiny Al (0.05 at.%) addition shows the optimum high-temperature oxidation resistance at 1500 °C.

Fig. 17 shows the oxide layer thickness variation curves of $Mo(Si_{1-x}Al_x)_2$ ($x = 0$–0.1) ceramics. Due to the failure and fragmentation of Mo $(Si_{0.85}Al_{0.15})_2$ and $Mo(Si_{0.8}Al_{0.2})_2$ ceramics after oxidation for 40–50 h, their mass change curves were not considered. It can be seen that the oxide layer of $MoSi_2$ is relatively thin, with a thickness of only 7.22 μm after 100 h of oxidation. The thin oxide layer is hard to effectively block the high-temperature diffusion of oxygen. For $Mo(Si_{0.95}Al_{0.05})_2$, the oxide layer thickness is 31.51 μm after 100 h, which is relatively higher than that of $MoSi_2$, indicating that this oxide layer can serve as a good barrier to prevent oxygen penetration and further oxidation of the interior ceramic. After 100 h of oxidation, the oxide layer thickness of $Mo(Si_{0.9}Al_{0.1})_2$ reaches 124.88 μm and a silicon-depleted layer (52.63 μm) also exists under the oxide layer. This indicates that excessive formation of the silicon-depleted layer results in a decrease in the overall high-temperature oxidation resistance of the ceramic. Although thick oxide layer is obtained by the oxidized $Mo(Si_{0.9}Al_{0.1})_2$, the formation of silicon-depleted layer with relatively higher thickness lead to more consumption of the ceramic under the same oxidation conditions, thereby reducing the overall oxidation resistance. In conclusion, the Mo $(Si_{0.95}Al_{0.05})_2$ ceramic exhibits moderate oxide layer thickness with minimal mass gain, effectively blocking high-temperature oxygen penetration. Therefore, $Mo(Si_{0.95}Al_{0.05})_2$ ceramic possesses the optimum high-temperature oxidation resistance.

4. Conclusions

A novel two-step technique of self-propagating high-temperature synthesis (SHS) and spark plasma sintering (SPS) was successfully applied in the synthesis of Al-alloyed $Mo(Si_{1-x}Al_x)_2$ ($x = 0$–0.2) powders and preparation of ceramics. After SHS, only the $MoSi_2$ phase was observed in $MoSi_2$ powder, while the Al-alloyed powders showed high-purity $Mo(Si,Al)_2$ phases, indicating the target phase was successfully synthesized by SHS. After the high-temperature SPS process, although microcracks could be observed in single $MoSi_2$ ceramics, the Al-alloyed ceramics showed compact and crack-free morphologies. After oxidation at 1500 °C, $MoSi_2$ mainly consisted of uncreated $MoSi_2$ phase and formed SiO_2 phase. By adding Al, the main phases in $Mo(Si_{1-x}Al_x)_2$ ($x =$ 0.05, 0.1, 0.15, 0.2) were $Mo(Si,Al)_2$, Al_2O_3 and SiO_2 phase, and the partial replacement of Si by Al improved the oxidation resistance of $MoSi_2$ due to the in-situ formation of protective Al-Si-O oxide layers. After long-term oxidation at 1500 °C (100 h), the ceramics with trace Al addition ($Mo(Si_{0.95}Al_{0.05})_2$) maintained a stable and slow mass gain, while failure happened in the Al-alloyed with excessive Al addition since higher Al content caused the transformation of $Mo(Si,Al)_2$ into an orthorhombic C54 structure, thereby worsening the oxidation resistance. Among all the prepared ceramics, the $Mo(Si_{0.95}Al_{0.05})_2$ ceramic exhibited dense morphology and stable mass change with continuous and compact Al-Si-O composite oxide layer, thus demonstrating excellent oxidation resistance at elevated temperatures.

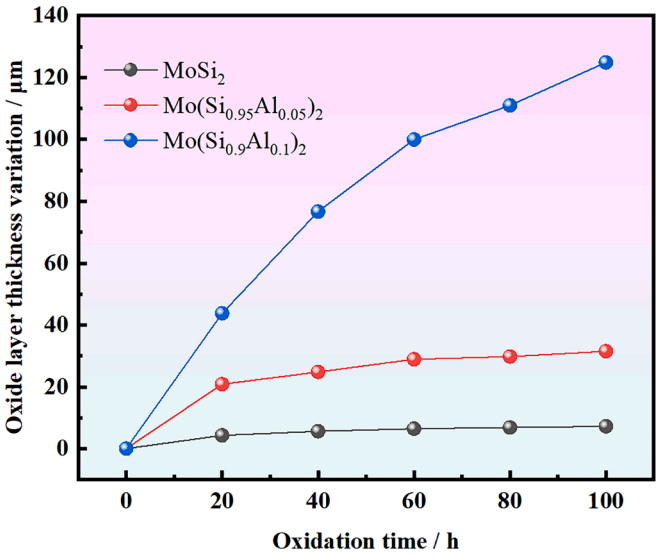

Fig. 17. Variation curve of the oxide layer thickness of $Mo(Si_{1-x}Al_x)_2$ ($x =$ 0–0.1) ceramics after oxidation at 1500 ℃ for 100 h.

CRediT authorship contribution statement

Nana Zhu: Writing – review & editing, Writing – original draft, Investigation. **Lu Zhu:** Writing – review & editing, Supervision, Methodology. **Baojing Zhang:** Supervision, Methodology, Conceptualization. **Peizhong Feng:** Writing – review & editing, Supervision, Project administration, Methodology, Funding acquisition, Conceptualization. **Shiheng Li:** Methodology, Conceptualization. **Philipp V. Kiryukhantsev-Korneev:** Methodology, Investigation, Conceptualization. **Evgeny A. Levashov:** Resources, Investigation. **Xuanru Ren:** Methodology, Conceptualization. **Xiaohong Wang:** Supervision, Resources, Investigation.

Declaration of competing interest

The authors declare that they have no known competing financial interests or personal relationships that could have appeared to influence the work reported in this paper.

Acknowledgements

This research was financially supported by the National Natural Science Foundation of China (No. 52474446, 52261135546, 51874305). E.A. Levashov would like to acknowledge the financial support by the Russian Science Foundation (Project No. 23-49-00141). We are grateful to the Advanced Analysis & Computation Center of China University of Mining and Technology.

Data availability

No data was used for the research described in the article.

References

[1] X. Ren, J. Lv, W. Li, Y. Hu, K. Sun, C. Ma, H. Chu, W. Wang, L. Xu, Z. Li, P. Feng, Influence of $MoSi_2$ on oxidation protective ability of TaB_2–SiC coating in oxygen-containing environments within a broad temperature range, J. Adv. Ceram. 9 (6) (2020) 703–715.

[2] J. Huang, G. Zhang, Microstructures and performances of pressureless sintered $MoSi_2$-Al_2O_3 composites, Corros. Sci. 224 (2023) 111514.

[3] F. Tao, Y. Zhang, L. Chen, F. Shen, J. Zhu, Micromorphology evolution, growth mechanism, and oxidation behaviour of the silicon-rich $MoSi_2$ coating at 1200 °C in air, J. Mater. Res. Technol. 29 (2024) 491–503.

[4] Z. Ding, J. Brouwer, C. Kwakernaak, M. Hermans, V. Popovich, W. Quadakkers, W. Sloof, Selective oxidation of aluminum in $Mo(Al,Si)_2$, Corros. Sci. 211 (2023) 110884.
[5] L. Ingemarsson, K. Hellstrom, L. Johansson, M. Halvarsson, Oxidation behaviour of a $Mo(Si,Al)_2$ based composite at 1500 °C, Intermetallics 19 (2011) 1319–1329.
[6] A. Stergiou, P. Taskiropoulos, A. Brown, The intermediate and high-temperature oxidation behaviour of $Mo(Si_{1-x}Al_x)_2$ intermetallic alloys, Intermetallics 5 (1997) 69–81.
[7] T. Maruyama, K. Yanagihara, High temperature oxidation and pesting of $Mo(Si,Al)_2$, Mater. Sci. Eng. A 239–240 (1997) 828–841.
[8] A. Stergiou, P. Tsakiropoulos, The intermediate and high-temperature oxidation behaviour of $(Mo,X)Si_2$ (X = W, Ta) intermetallic alloys, Intermetallics 5 (1997) 117–126.
[9] E. Strom, Y. Cao, Y. Yao, Low temperature oxidation of Cr-alloyed $MoSi_2$, Trans. Nonferrous Met. Soc. Chin. 17 (2007) 1282–1286.
[10] C. Ramberg, W. Worrell, Oxidation kinetics and composite scale formation in the system $Mo(Al,Si)_2$, J. Am. Ceram. Soc. 85 (2) (2002) 444–452.
[11] T. Tabaru, K. Shobu, H. Hirai, S. Hanada, Influences of Al content and secondary phase of $Mo_5(Si,Al)_3$ on the oxidation resistance of Al-rich $Mo(Si,Al)_2$-base composites, Intermetallics 11 (2003) 721–733.
[12] D. Yao, J. Yang, W. Gong, C. Zhou, Interdiffusion behavior between Nb and $MoSi_2$ intermetallic compound, Mater. Sci. Eng. A 527 (2010) 6787–6793.
[13] L. Xiao, X. Zhou, Y. Wang, R. Pu, G. Zhao, Z. Shen, Y. Huang, S. Liu, Z. Cai, X. Zhao, Formation and oxidation behavior of Ce-modified $MoSi_2$-$NbSi_2$ coating on niobium alloy, Corros. Sci. 173 (2020) 108751.
[14] N. Li, J. Gao, W. Wang, S. Chen, K. Wang, Y. Wang, C. Wen, H. Sun, Oxidation resistance of Cr-modified $MoSi_2$ composites at high temperature, Int. J. Refract Metal Hard Mater. 119 (2024) 106497.
[15] Z. Chen, W. Shao, M. Li, Z. Wu, P. Peng, C. Zhou, Effect of minor B modification on the oxidation behavior of $MoSi_2$ alloy at high temperature, Corros. Sci. 216 (2023) 111070.
[16] O. Zhu, L. Zhang, J. Yu, A. Shan, J. Wu, K. Hagihara, T. Nakano, Effects of Cr-addition and lamellar microstructure on the oxidation behavior of single crystal $(Mo_{0.85}Nb_{0.15})Si_2$, J. Alloy. Compd. 509 (2011) 1511–1516.
[17] R. Mitra, V. Rao, Effect of minor alloying with Al on oxidation behaviour of $MoSi_2$ at 1200 °C, Mater. Sci. Eng. A 260 (1999) 146–160.
[18] S. Majumdar, I. Sharma, S. Raveendra, I. Samajdar, P. Bhargava, In situ chemical vapour co-deposition of Al and Si to form diffusion coatings on TZM, Mater. Sci. Eng. A 492 (2008) 211–217.
[19] L. Wu, J. Wu, W. Wu, G. Hou, H. Cao, Y. Tang, High temperature oxidation resistance of γ-TiAl alloy with pack aluminizing and electrodeposited SiO_2 composite coating, Corros. Sci. 146 (2019) 18–27.
[20] E. Juarez-Arellano, A. Martinez-Garcia, B. Winkler, T. Pérez-López, J. Padilla, Parametrization of the mechanically induced self-propagating high-temperature synthesis (MI-SHS) of Ti_5Si_3, Ceram. Int. 49 (2023) 2350–2358.
[21] K. Guan, W. Lei, H. Wang, X. Liu, J. Luo, J. Liu, Q. Jia, H. Zhang, S. Zhang, Efficient synthesis of Ti_3AlC_2 powders with high purity by microwave-assisted molten salt method, Ceram. Int. 48 (2022) 16357–16363.
[22] H. Dan, L. Chen, Z. Li, X. He, Y. Ding, Preparation of amorphous ZrO_2 powders by hydrothermal-assisted sol-gel method, Inorg. Chem. Commun. 138 (2022) 109272.
[23] B. Han, N. Li, Preparation of b-SiC/Al_2O_3 composite from kaolinite gangue by carbothermal reduction, Ceram. Int. 31 (2005) 227–231.
[24] C. Yeh, W. Chen, Combustion synthesis of $MoSi_2$ and $MoSi_2$–Mo_5Si_3 composites, J. Alloy. Compd. 438 (2007) 165–170.
[25] K. Naplocha, Self-propagating high-temperature synthesis (SHS) of intermetallic matrix composites, Intermetallic Matrix Composites (2018) 203–220.
[26] T. Fu, Z. Han, Y. Zhang, S. Zhan, L, Chen, J, Zhu, Low-temperature oxidation behavior and mechanism of hot-dip Al and Al-Si coatings on Mo substrate at 600 °C in static air, Int. J. Refract Metal Hard Mater. 124 (2024) 106831.
[27] Y. Zhang, T. Fu, L. Yu, F. Shen, J. Wang, K. Cui, Improving oxidation resistance of TZM alloy by deposited Si–$MoSi_2$ composite coating with high silicon concentration, Ceram. Int. 48 (14) (2022) 20895–20904.
[28] V. Pasagada, N. Yang, C. Xu, Electron beam sintering (EBS) process for ultra-high temperature ceramics (UHTCs) and the comparison with traditional UHTC sintering and metal electron beam melting (EBM) processes, Ceram. Int. 48 (2022) 10174–10186.
[29] Z. Tang, M. Yi, H. Wu, Y. Zhou, R. Liu, J. Jiang, K. Peng, A novel approach for preparing a SiC coating on a C/C-SiC composite by slurry painting and chemical vapor reaction, J. Eur. Ceram. Soc. 42 (2022) 1884–1892.
[30] B. Li, H. Li, X. Yao, Ablation behaviour of the CVD-$(ZrC/SiC)_3$ alternate coating on C/C composites under oxyacetylene torch with different heat fluxes, Ceram. Int. 48 (2022) 11756–11763.
[31] J. Pourasad, N. Ehsani, Z. Valefi, S. Khalifesoltani, Preparation of a nanostructured SiC-ZrO_2 coating to improve the oxidation resistance of graphite, Surf. Coat. Technol. 323 (2017) 58–64.
[32] S. Zhao, X. Song, J. Zhang, X. Liu, Effects of scale combination and contact condition of raw powders on SPS sintered near-nanocrystalline WC–Co alloy, Mater. Sci. Eng. A 473 (2008) 323–329.
[33] T. Fu, Y. Zhang, F. Shen, K. Cui, L. Chen, Microstructure and oxidation behavior of Si-$MoSi_2$ coating deposited on Mo substrate at 600 ℃ and 900 ℃ in static air, Mater Charact 192 (2022) 112192.
[34] P. Wang, S. Zhou, P. Hu, G. Chen, X. Zhang, W. Han, Ablation resistance of ZrB_2-SiC/SiC coating prepared by pack cementation for graphite, J. Alloy. Compd. 682 (2016) 203–207.
[35] L. Zhu, S. Zhang, F. Ye, X. Ren, P. Feng, Recycling of $MoSi_2$-based industrial solid wastes for the fabrication and high-temperature oxidation behavior of $MoSi_2$–$ZrSi_2$–SiC composite coating, Compos. B 274 (2024) 111281.
[36] S. Guo, T. Mizuguchi, M. Ikegami, Y. Kagawa, Oxidation behavior of ZrB_2–$MoSi_2$–SiC composites in air at 1500 °C, Ceram. Int. 37 (2011) 585–591.
[37] J. Sun, Q. Fu, C. Huo, T. Li, C. Wang, C. Cheng, G. Yang, J. Sun, Oxidation response determined by multiphase-dependent melting degree of plasma sprayed $MoSi_2$ on Nb-based alloy, J. Alloy. Compd. 762 (2018) 922–932.
[38] Q. Zhu, W. Ji, J. Zou, W. Wang, W. Guo, J. Fang, H. Lin, Z. Fu, Strengthening $Hf_{0.95}Ta_{0.05}B_2$ ceramic with ultrafine grains and high-density dislocations, J. Eur. Ceram. Soc. 43 (2023) 6599–6605.
[39] Z. Ding, J.C. Brouwer, X. Yao, J. Zhu, M.J.M. Hermans, V. Popovich, W.G. Sloof, On the high temperature oxidation of $MoSi_2$ particles with boron addition, J. Eur. Ceram. Soc. 44 (2024) 7170–7179.
[40] S.H. Wen, J.B. Sha, Isothermal and cyclic oxidation behaviours of $MoSi_2$ with additions of B at 1250 °C prepared by spark plasma sintering, Mater Charact 139 (2018) 134–143.
[41] L. Nisa, B. Hermanto, S. Aritonang, M. Manawan, T. Sudiro, Mechanical properties and high-temperature oxidation of (WC-12Co) +$MoSi_2$ hardmetals, Int. J. Refract Metal Hard Mater. 109 (2022) 105987.
[42] J. Arreguín-Zavala, S. Turenne, A. Martel, A. Benaissa, Microwave sintering of $MoSi_2$–Mo_5Si_3 to promote a final nanometer-scale microstructure and suppressing of pesting phenomenon, Mater Charact 68 (2012) 117–122.
[43] P. Krakhmalev, E. Strom, M. Sundberg, C. Li, Microstructure, hardness and indentation toughness of high-temperature C40 $Mo(Si,Al)_2$/SiC composites prepared by SPS of MA powders, Mater. Lett. 57 (2003) 3387–3391.
[44] Z. Munir, U. Anselmi-Tamburini, Self-propagating exothermic reactions: the synthesis of high-temperature materials by combustion, Materials Science Reports. 3 (7) (1989) 277–36557.
[45] A. Merzhanov, The chemistry of self-propagating high-temperature synthesis, J. Mater. Chem. 14 (2004) 1779–1786.
[46] L. Jia, H. Xie, Z. Liu, C. Zhang, Microstructure evolution of Mo–Si–Al system during self-propagation high-temperature synthesis, selective oxidation of aluminum in $Mo(Al,Si)_2$, J. Alloy. Compd. 554 (2013) 127–131.
[47] M. Ghayoumabadi, A. Saidi, M. Abbasi, Lattice variations and phase evolutions during combustion reactions in Mo–Si–Al system, J. Alloy. Compd. 472 (2009) 84–90.
[48] P. Frankwicz, J. Perepezko, Phase stability of $MoSi_2$ in the C11b and C40 structures at high temperatures, Mater. Sci. Eng. A 246 (1998) 199–206.
[49] Y. Liu, G. Shao, P. Tsakiropoulos, Thermodynamic reassessment of the Mo-Si and Al-Mo-Si systems, Intermetallics 8 (2000) 953–962.
[50] Y. Zhang, L. Yu, T. Fu, J. Wang, F. Shen, K. Cui, H. Wang, Microstructure and oxidation resistance of Si-$MoSi_2$ ceramic coating on TZM (Mo-0.5Ti-0.1Zr-0.02C) alloy at 1500 ℃, Surf. Coat. Technol. 431 (2022) 128037.
[51] H. Jiang, Y. Qiao, W. Zhang, X. Guo, Characterization of microstructure and oxidation behavior of Al modified $MoSi_2$ coating on Nb-Si based alloy, Surf. Interfaces 51 (2024) 104739.
[52] T. Tabaru, K. Shobu, M. Sakamoto, S. Hanada, Effects of substitution of Al for Si on the lattice variations and thermal expansion of $Mo(Si,Al)_2$, Intermetallics 12 (2004) 33–41.
[53] H. Yang, Y. Pei, J. Hosson, Oxide-scale growth on Cr_2AlC ceramic and its consequence for self-healing, Scr. Mater. 69 (2013) 203–206.
[54] J. Nychka, D. Claeke, Quantification of aluminum outward diffusion during oxidation of FeCrAl alloys, Oxid. Met. 63 (5) (2005) 325–352.
[55] V. Tolpygo, D. Clarke, Microstructural evidence for counter-diffusion of aluminum and oxygen during the growth of alumina scales, Mater. High Temp. 20 (2003) 261–271.
[56] M. Zhang, X. Ren, M. Zhang, S. Wang, L. Wang, Q. Yang, H. Chu, P. Feng, Preparation of ZrB_2-$MoSi_2$ high oxygen resistant coating using nonequilibrium state powders by self-propagating high-temperature synthesis, J. Adv. Ceram. 10 (5) (2021) 1011–1024.
[57] A. Edgren, E. Strom, A. Rajagopal, M. Colliander, Alloying of C40-structured $Mo(Si,Al)_2$ with Nb, Ta and V, Materials Letters. 353 (2023) 135219.